Welding in the World
https://doi.org/10.1007/s40194-026-02402-5

RESEARCH PAPER

Resistance welding for future hydrogen economy—the comeback of an old welding technology for modern applications

Maike Epperlein[1] · Martin Aretz[2] · Alexander Schiebahn[1] · Uwe Reisgen[1]

Received: 30 September 2025 / Accepted: 15 February 2026

Abstract
Upscaling hydrogen production through water electrolysis with proton exchange membranes (PEM) has established high interest in several industrial fields to achieve the ambitious goals given by legislative bodies regarding production volumes and cost reductions. One approach is the substitution of sintered bodies with joined multi-layered expanded metal mesh (EMM) composites that are used as porous transport layers in PEM electrolysis. For joining the multi-layered structures, capacitor discharge welding is a favored welding technology, which offers the possibility for automation, while being a highly economic and robust process. But since EMM exhibits anisotropic properties as well as a wide variety of mesh geometries, the design of such multi-layered composites leads to various possibilities for modifying the properties of the composites in terms of flow characteristics and cell efficiency. Simultaneously, these variations also influence the joining process itself. In this paper, different EMM geometries are joined in 90°- and 180°-layer-to-layer orientation in a resistance projection welding process with capacitor discharge welding. While compression tests reveal improved damping characteristics for 90°-orientation, the CFD simulation hints at more pronounced turbulences in fluid flow which are assumed to favor gas bubble accumulation and a cell efficiency decrease. Contrary, for 180°-orientation less flow turbulences and a smaller pressure drop across the cell are revealed.

Keywords Resistance projection welding · Hydrogen economy · PEM-electrolysis · Porous transport layer · CFD simulation · Fluid dynamics

1 Introduction

Proton exchange membrane (PEM) electrolysis has been established as a promising technology for hydrogen production, particularly for the energy transition and the development of sustainable energy systems. In PEM electrolysis, water is split into hydrogen (H_2) and oxygen (O_2) when applying an electric current. Among other electrolysis methods, PEM electrolysis is focused on because of the ability to produce *green hydrogen*. *Green hydrogen* is hydrogen that is produced with renewable energy only. By using renewable energies, e.g., solar energy, for power supply of the electrolyzer, PEM electrolysis is low in carbon emissions and goals in mitigation of climate change are facilitated when decarbonizing industries and manufactures. But, in order to do so, the upscaling of PEM electrolysis and its production chain can be seen as major step for the realization of a sustainable energy system as such, which in turn makes the costs for green hydrogen affordable [1, 2].

Crucial components of this technology are the porous transport layers (PTL), which play an essential role in the efficiency and performance of an electrolyzer. These layers not only serve as mechanical support for the membrane, but also enable the effective transport of the gaseous reaction products as well as the distribution of the water [3].

While sintered bodies were the material of choice for PTL in PEM electrolysis under laboratory conditions (controlled porosity and good mechanical stability), the need for

Recommended for publication by Commission III - Resistance Welding, Solid State Welding, and Allied Joining Process

✉ Maike Epperlein
maike.epperlein@isf.rwth-aachen.de

Martin Aretz
martin.aretz@ipt.fraunhofer.de

[1] Welding and Joining Institute, RWTH Aachen University, Pontstraße 49, 52062 Aachen, Germany

[2] Fraunhofer Institute for Production Technology, Steinbachstraße 17, 52074 Aachen, Germany

Published online: 03 March 2026

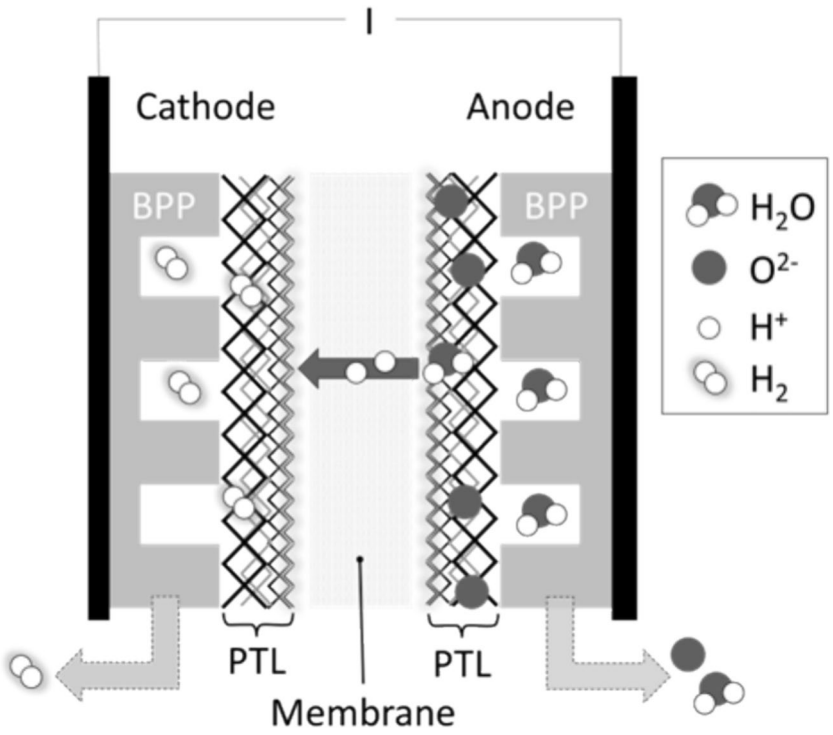

Fig. 1 Schematic depiction of water electrolysis principle in a PEM cell extended according to [10]

upscaling the electrolyzer production while simultaneously reducing production costs inhibits the use of sintered bodies. Sintering is a thermal process, in which powder materials are heated to form a compound through activated diffusion processes between the particles. Through compression, the porosity can be adjusted individually. But a high energy consumption and high cycle times for heating make sintering unfavored for an upscaled, economic PEM electrolyzer production. A more economic method is expanded metal mesh (EMM) joined through capacitor discharge welding to form a multi-layered composite. In terms of cost-effectiveness, joining EMM in a resistance projection welding process offers clear advantages over alternative joining processes, e.g., diffusion welding. In addition to short process times in the millisecond range, resistance welding is a robust welding process which is easy to automate and can therefore be easily integrated into upscaled production lines [4]. In Addition, the amount of oxidation which is visible as temper coloring on the composite can be significantly reduced [5].

Current research is mainly focused on single layered EMM applications as PTL, for PEM-EL and PEM fuel cells, but also for direct methanol fuel cells. Still, literature on research regarding multi-layered metal mesh composites used as PTL and its effect on cell performance is hard to find. It is already reported that mesh geometry and orientation in a PEM cell have a significant effect on cell efficiency, e.g., when reducing the mass transport because of a favored but unwanted bubble accumulation when using single EMM-layers as PTL [6–8].

Increasing the number of layers is expected to change previously reported results significantly, through a combination of a fine EMM, which is positioned towards the polymer membrane for mechanical stabilization, with coarser EMM for enhanced medium transport and gas bubble permeability. But since EMMs not only come in different sizes with individually variable mesh geometry, the stacking of the EMM layers can also affect the overall properties of the PTL through changing two-phased transport characteristics, mass transport, and electric conductivity.

1.1 PEM electrolysis

Electrolysis is the forced decomposition of a molecule into its individual components due to an applied electric current. In hydrogen electrolysis, three main technologies are distinguished. In *alkaline electrolysis*, which is the oldest technique and the most sophisticated one with a technology readiness level (TRL) of seven to nine, mainly potassium hydroxide (KOH) or sodium hydroxide (NaOH) are used as alkaline liquid electrolyte. The *high temperature electrolysis*, in which water, i.e., water steam, is used as electrolyte and operating temperatures up to 900 °C are applied, is not available in high volumes and TRL reaches from 4 to 8 with regard to different subtypes. Contrary, water electrolysis with *proton exchange membrane (PEM)* is a promising technique in which high purity hydrogen can be produced with an efficiency up to 90% in a compact system design [9]. Figure 1 depicts the cell components and the principle of

PEM electrolysis schematically with a polymer membrane that is permeable for protons (H^+).

In PEM electrolysis, the polymer membrane is enclosed between two porous transport layers (PTL), which in turn are in direct contact with the bipolar plate (BPP), which defines the water inflow via integrated channel structures. The cell is flooded with deionized water, which provides bonded hydrogen atoms and keeps the membrane humidified for maintaining a high proton conductivity. When applying an electric current, two water molecules are split into 4 H^+, oxygen (O_2), and 4 electrons ($e.^-$) at the anode. The protons diffuse through the polymer membrane because of an ion exchange mechanism and are transported from the membrane through the PTL into the BPP on cathode side. The oxygen remains on anode side and leads to a local oxidative environment. This highly oxidative environment requires the need for corrosion resistant base materials, e.g., titanium, for PEM cell components, especially on the anode side. In addition, porosity and pore size distribution, flow characteristics of the medium, and thickness need to be optimized to ensure a high cell efficiency with a sufficient two-phased media transport (water, gaseous oxygen, and hydrogen), good electric and thermal conductivity, and the required mechanical stability (clamping of the cell). Next to cost effective base materials, catalytic materials are required for the activation of the hydrogen evolution reaction (HER) on cathode side and oxygen evolution reaction (OER) on anode side. Therefore, the membrane is coated with catalysts that decrease the respective activation overpotential which is needed for the reactions to take place. On cathode side, platinum is commonly used while iridium oxide (IrO_2) or ruthenium oxide (RuO_2) are applied on anode side [3, 10, 11].

1.2 Expanded metal mesh

In expanded metal manufacturing process, rolled sheet material is partially cut and deformed plastically to increase rigidity and area while saving material [12]. Figure 2 depicts the process steps in expanded metal manufacturing.

In the first step, the rolled sheet is partially cut with a tool which is alternately moved vertically and sideways to form expanded metal with defined mesh geometry (Fig. 2, step 1). In one vertical tool movement, one half of the rhombus in first line is formed. Each cycle consists of this vertical movement, downwards and upwards, followed by a sheet feed (distance equals half of the mesh width) and a tool movement sideways (distance equals half of the mesh length). After a second vertical tool movement in which the neighboring rhombus is cut, the cycle ends with a sheet feed and a movement sideways to end at the initial tool position. Depending on the tool geometry and the choice of process parameters, e.g., feed and speed of tool movement, mesh geometry can be varied in size and

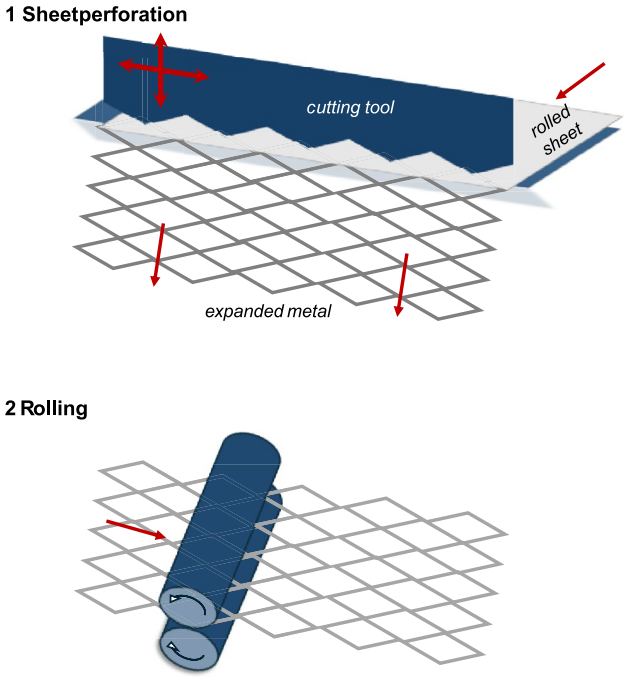

Fig. 2 Steps of expanded metal manufacturing process [12]

shape. Typical mesh types are rhombus, round or hexagonal shaped meshes. Compared to the rolled sheet, the semi-finished product is elongated, while plastic deformation leading to an increase in dislocation density leads to an increase in strain hardening. In the second production step, the expanded metal sheet is rolled to adjust the overall height. In addition, distortion resulting from internal stresses due to the first production step can be reduced and therefore, the quality of the semi-finished product can be increased. [12] In Fig. 3, the geometric parameters of EMM are depicted in a schematic front and side view of an EMM.

Regarding the use as PTL, EMM has several advantages over sintered bodies, although the latter offers an adjustable porosity and complex flow network which directly influences the mass transfer and mechanical stability. Wang et al. [14] summarized the advantages of EMM as "lightweight, easy-to-make, high open ratio and good mechanical strength." In addition, the process reduces material waste since no material is lost [14] and can easily be implemented in roll-to-roll production lines.

1.3 CD welding of PEM cell components

With regard to an upscaled series production and the need for a higher cost efficiency in electrolysis cell production, sintered bodies are less convenient because of long production times and high process energy requirements. An alternative is PTLs composed of multiple EMM with different

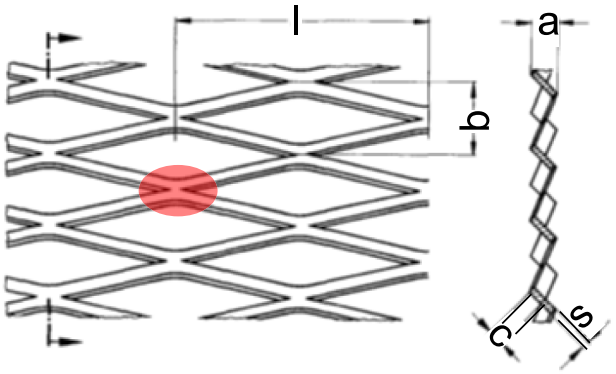

Fig. 3 Schematic depiction of front and side view of EMM, with mesh length *l*, mesh width *b*, height *a*, bridge width *s*, and bridge height *c*, mesh knot marked in red [13]

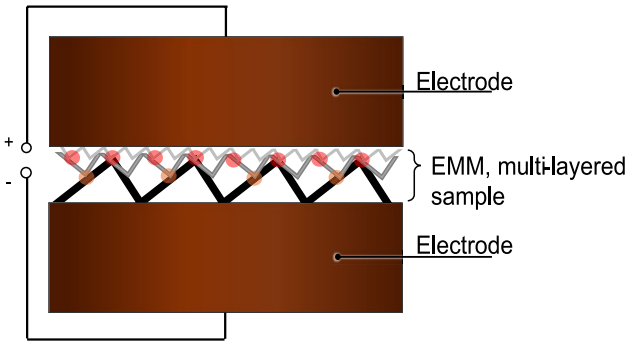

Fig. 4 Schematic depiction of resistance welding process of multi-layered EMM, with varying number of natural projections in each joint plane

mesh sizes. Instead of only stacking and clamping the layers (high contact resistance), joining the different layers to form multi-layered composites with material continuity offers the possibility to decrease the electric resistance of the PTL, increase the electric conductivity and hence increase cell performance through improving current flow characteristics throughout the cell.

In this context, resistance welding, i.e., projection welding, with capacitor discharge is an attractive welding technology, which is known for its high economic efficiency because of cycle times within the milli second range, a good reproducibility and a high automatability [4]. Figure 4 depicts the process principle of projection welding with capacitor discharge using the example of joining multi-layered structures in one step.

In projection welding, the components are contacted and fixated from two sides with electrodes, which also conduct the welding current into the joining partners. According to Joule's law, most heating occurs at the point of highest resistance, which is the contact area between the joining partners (Fig. 4).

In the present joining task, the strands of the EMM (Fig. 3) serve as natural projections, which define the welding current pathway from one layer to the following. In each joining plane, the local welding current density is defined by the contact area, which can vary depending on the number of contact points that result from mesh orientation, offset, size, and deformation.

Regarding the high-quality standards required for PEM cell components, the following requirements for the projection welding process can be derived:

- After welding, the PTL has to have a high electric conductivity, achieved by a good joint connection of all layers and no or highly limited oxide formation during the welding of titanium mesh, because the insulating effect of oxides goes hand in hand with a decrease in conductivity (increased electric resistance) and therefore a decrease in cell efficiency, as well as an increase in degradation risk through a reduced corrosion resistance [10, 15, 16].
- Especially the side that is faced towards the membrane and catalyst layer, respectively, has to have a high corrosion resistance [10, 17].
- No mesh collapses through mechanical overload or severe spatter formation during welding because of possible resulting changes in flow characteristics, which can lead to a deterioration of the two-phase transport (water, gas) and losses in mass transport [18–21].
- After welding, the joints must have suitable mechanical stability to withstand compressive stresses at approximately 2.5 MPa, which are determined as the range of highest cell efficiency. Heat input should be as low as possible to avoid reduced strength, corrosion resistance, and embrittlement [18, 22, 23].

As described in previous work, resistance welding with capacitor discharge technology can significantly reduce the formation of Ti-oxides during welding procedure because of the very short welding times [5]. But, the required welding parameters are highly dependent on the composite structure, i.e., the contact area in each joint plane, which is given by the EMM geometry and stacking of the different layers. It is reported that the fine EMM is the least to be joined and is the one influencing the welding lobe most significantly [5].

In this paper, two different EMM geometries are joined in a resistance projection welding process with capacitor discharge technology to form three-layered composites. Doing so, two stacking variations with different EMM orientations are applied. The joined composites are tested

Table 1 Alloy composition of used base material according to material certificate [24]

	Fe	C	N	H	O	Residuals each	Residuals total	Ti
Max [mass-%]	0.20	0.08	0.03	0.015	0.18	0.10	0.40	Balance
Result [mass-%]	0.053	0.027	0.006	0.002	0.068	< 0.10	< 0.40	Balance

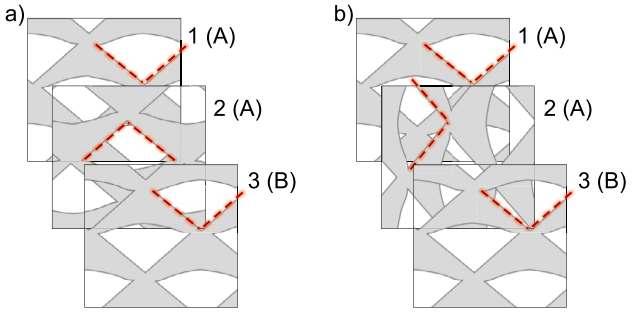

Fig. 5 Schematic depiction of EMM adjustment with 180° stack-up (**a**) and 90° stack-up (**b**) of type A and B

Table 2 Geometries *A* and *B* of the used EMM geometries

Type	LWD [mm]	SWD [mm]	Height [mm]
A	4.0	2.0	1.0
B	0.6	0.5	0.1

to determine the mechanical stability and damping characteristics, electric resistivity, and fluid permeability. In addition, flow test results are supplemented by computational fluid dynamics simulation.

2 Methodology

Table 1 lists the chemical composition of the base metal titanium grade one according to the manufacturer's quality certificate of the material.

The EMM used in this work has diamond-like shaped meshes. In Table 2, the geometric values of the different EMM are listed. SWD stands for the short width diagonal of the diamond shaped meshes, LWD stands for the long width diagonal. In Fig. 5, the EMM stacking variations investigated for the three-layered test samples are presented.

In Fig. 5, the investigated EMM stack-up as a three-layered composite with 90° and 180° arrangement of the middle layer is shown.

With regard to mesh geometry, the middle layer is rotated clockwise by 180° or 90°, respectively (Fig. 5). The latter arrangement is patented [25]. In Fig. 6, the different sides of EMM with smooth (a) and rough (b) surface are depicted.

In this work, all EMM that are contained in the different orientation variations have the smooth side facing towards the rough side of the upper next EMM layer. That is, all smooth sides are facing towards the smallest mesh size which later is the EMM layer that is aligned towards the membrane. The square area of the sample is 42 mm × 42 mm (17.64 cm^2) and assumed to be the active cell area.

2.1 Determination of contact area

To compare the differences in the contact area between the different layers to one another, two-sheet indicator paper (FUJIFILM Europe GmbH) is used. In Fig. 7, the principle of the indicator paper is depicted schematically.

While one sheet is coated with color forming reactants, the second sheet is coated with a developer. Under load, the two coatings get in contact and react, and the reaction product is visible as a color change from white to red. The color change is proportional to the pressure experienced and enables a quantitative analysis. In this work, the indicator paper LLW–Super low pressure (LLW) with a pressure range of 0.5 MPa (light red) to 2.5 MPa (dark red) is used. With an analysis software, the contact areas of the different configurations are evaluated and compared to one another.

Figure 8 provides an overview of the procedure for the evaluation of the pressure distribution at the expanded metal structures.

The orientation dependent contact area is determined in a compression test. The pressure sensitive sheets are placed between two EMMs. For a defined force application, a universal testing machine equipped with two planar tool plates is used. After the compression test, the stained sheet and the determined pressure curve are used for evaluation of the pressure distribution. The stained sheets (red shading on white background) are scanned with a resolution of 45 µm side length per pixel. In conjunction with the calibration data sheets provided by the manufacturer, an evaluation of print values for each pixel proportional to the individual red color hue is enabled. Assuming an active area of 17.64 cm^2, the pressure distribution is displayed graphically in a 2D heat map (Fig. 8). It is noted that the real contact areas might differ from one another because of deviations in slicing of the EMM samples.

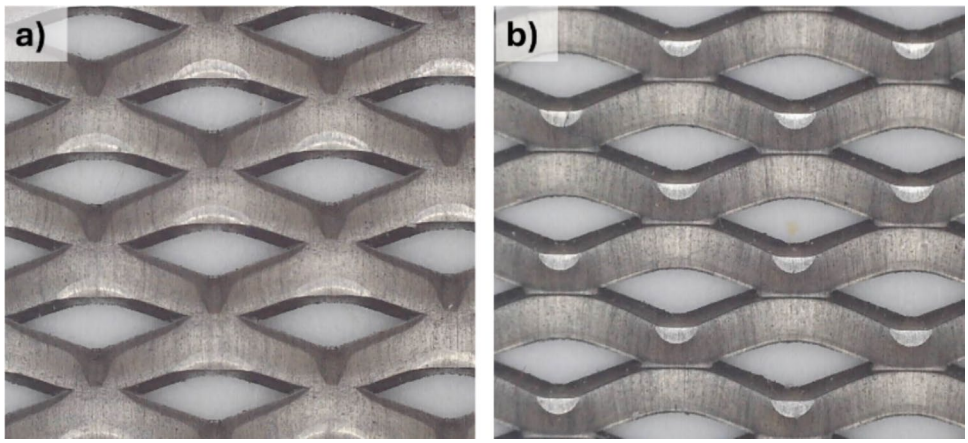

Fig. 6 Photographic depiction of smooth (**a**) and rough (**b**) side of EMM

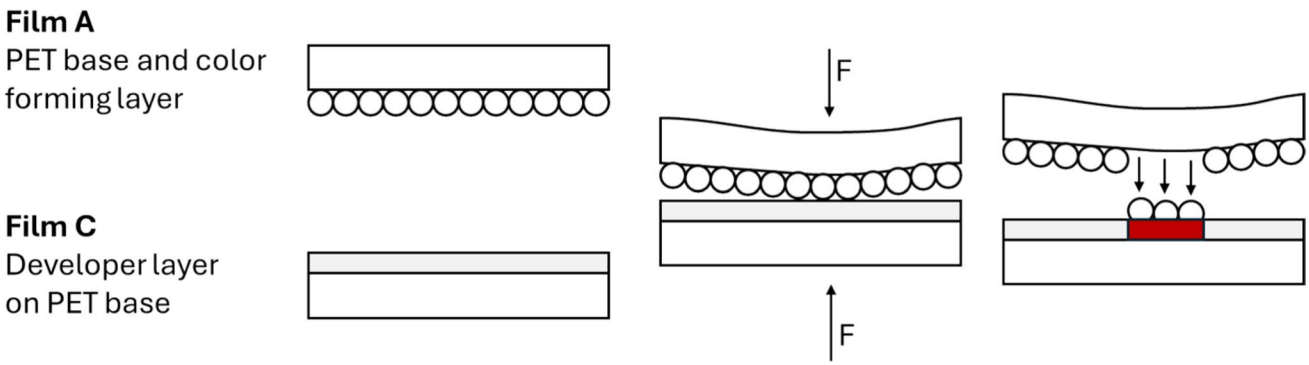

Fig. 7 Schematic depiction of principle of two-sheet indicator paper, extended according to [26]

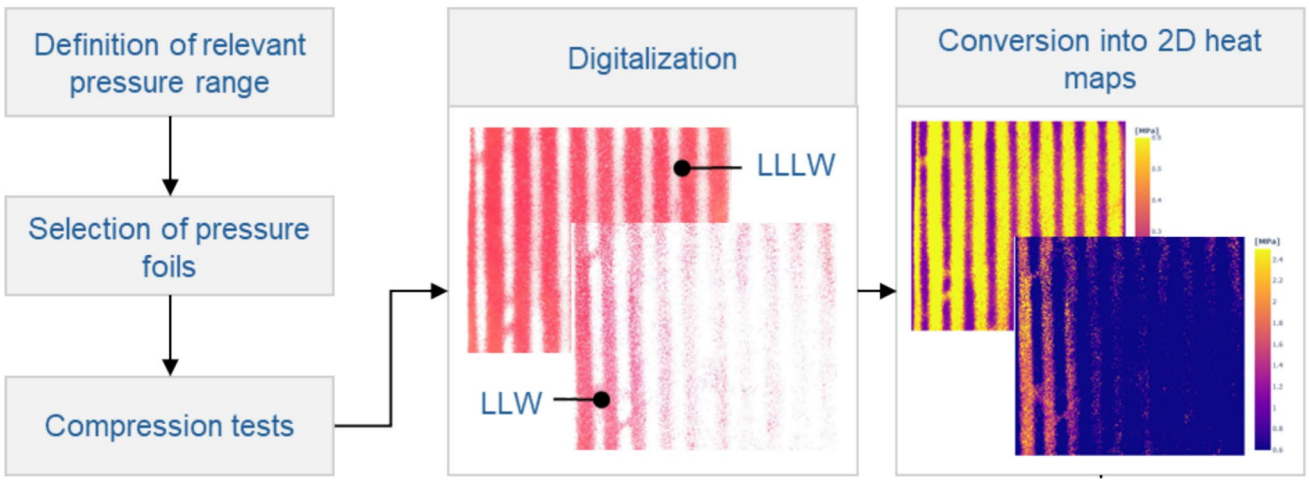

Fig. 8 Schematic depiction of the analysis steps when determining pressure distribution and orientation dependent contact area between two EMMs with indicator paper

2.2 Welding procedure

For welding, a capacitor discharge (CD) welding machine in portal construction with up to 20 kJ storage energy and 3.5 kV storage voltage (U_l) is used (Manfred Schlemmer GmbH).

The welding machine is equipped with a hydraulic force unit and four elastomer springs as follow-up unit.

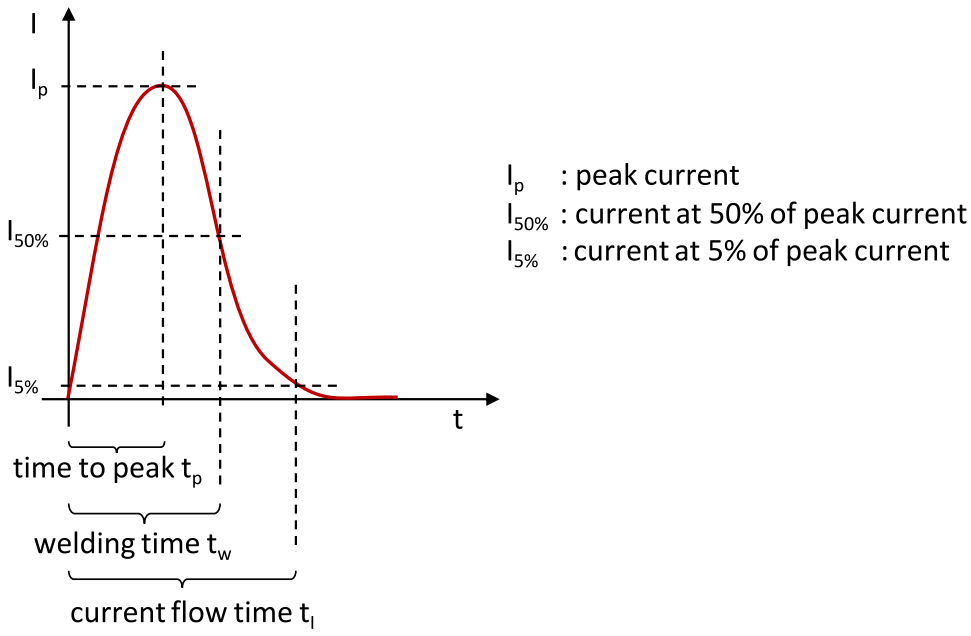

Fig. 9 Schematic depiction and definition of the welding current curve and relevant values [27]

Table 3 Welding parameter

Mid layer orientation	90°		180°	
Parameter set	*A*	*B*	*A*	*B*
F_i [kN]	7	7	7	7
F_{el} [kN]	15	15	15	15
Energy [%]	48	50	48	50
U_l [kV]	2.2	2.4	2.2	2.4
I_P [kA]*	178	181	184	188
t_P [ms]*	7	7	7	7
Voltage at $t=0$ ms [V]*	8.365	8.566	8.382	8.533

*Mean values determined from process data

The used electrodes are made of W80Cu20 and have a square work surface of 50 mm × 50 mm, and because of the expected long handling time, no water-cooling system is implemented in the electrodes.

The time-dependent current form and corresponding definitions in CD-welding are depicted in Fig. 9.

In CD welding, the welding current is not regulated; thus, welding current, secondary voltage, and welding time are a result of the transformation ratio and the inductance and resistance in the welding circuit.

After an iterative parameter determination, the parameter matrix is set up as presented in Table 3.

An initial electrode force of $F_i = 7$ kN is applied to bring the EMMs into contact. The electrode force of $F_{el} = 15$ kN is kept constant. Throughout the experiments, mesh B is placed towards the anode. The sample size is $n = 5$.

2.3 Electric resistance

For determination of the electric resistance, the test bench shown in Fig. 10 is used.

The measurement is carried out with regard to DVS 2929 [28]. The electrode geometry is equal to the one used during welding (Fig. 10), but the electrode base material is CuCr1Zr. The resistance measurements are carried out at different electrode force levels, starting from 1 up to 7 kN with 1 kN steps, and with unwelded and welded samples for 90°- and 180°-orientation, respectively. The resistance is measured after 5 s and for calculating the specific electric resistance, the total square area of 17.64 cm^2 is used. In the case of the welded samples, the sample height is measured with regard to the different force intervals, additionally.

2.4 Compression test

Compression tests are carried out with regard to DIN EN ISO 50106 [29] using a universal tensile/compression test machine with a maximum force of 20 kN. Before testing, the sample height is measured.

As depicted in Fig. 11, the tests are run with an automated test procedure including a time-dependent force profile.

After inserting the sample into the test bench, two hysteresis loops are performed. At first, the compression force is increased up to $F = 4.5$ kN (2.5 MPa) and relieved afterwards until $F = 0$ kN. For the second hysteresis, the Force is increased up to $F = 7$ kN (4 MPa) and again, released until $F = 0$ kN.

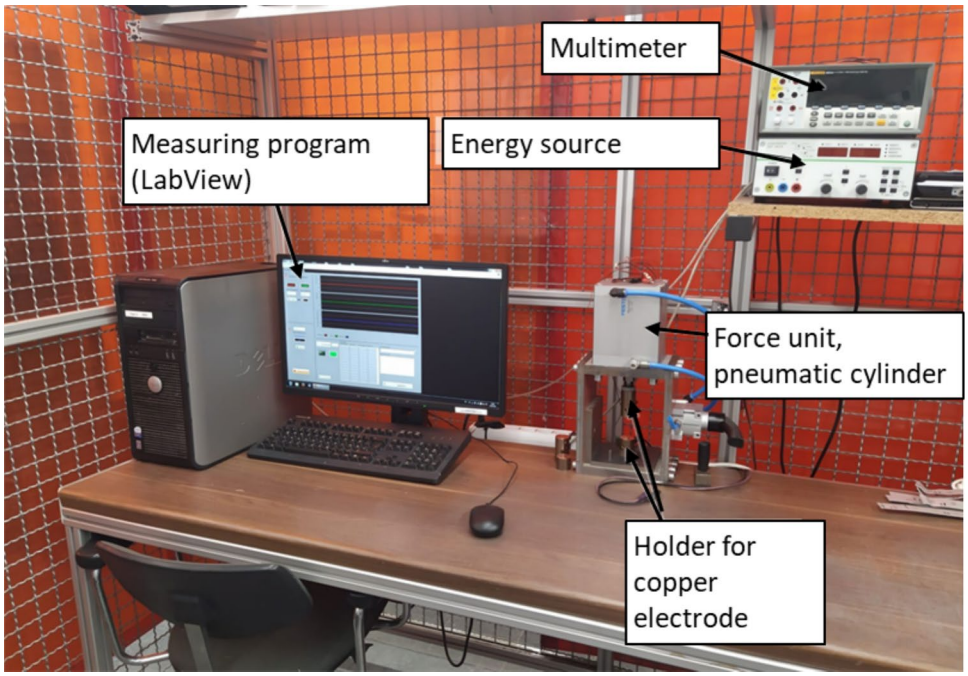

Fig. 10 Test bench at ISF for measurement of electric resistance

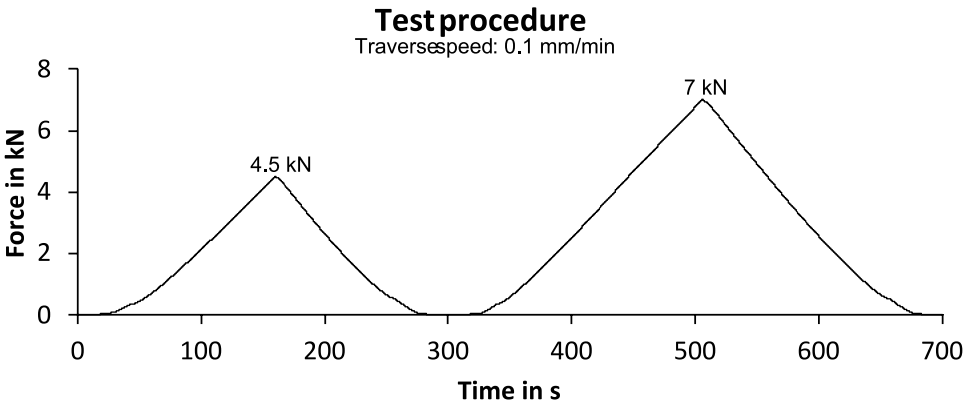

Fig. 11 Test procedure of compression tests with force over time

As a result, two hysteresis loops are received (force-displacement curves) for each sample which give information about the spring characteristics of the welded samples. Both hysteresis loops are evaluated separately. Next to Δs, which is the delta between displacement s before loading and after releasing the compression force, the work is calculated through calculating the area within the hysteresis loop.

2.5 Flow tests

For fluidical characterization of the welded multi-layered EMM composites, the test bench depicted in Fig. 12 is used. The included test cell consists of an aluminum base frame, an attached transparent cover plate which enables external visual test devices, and a pressure unit for the anode structure.

The cover plate, which also serves as a bipolar plate, is available in two versions, with and without flow channels. To be able to test different structure heights, the active testing area is variable in thickness. This allows expanded metal samples of different thicknesses to be tested in single or multiple layer arrangements. A cell size of 50 cm^2 is assumed for the fluidic design of the test stand. As test fluid, tap water is used and fed into the test cell using an electric gear pump and is discharged diagonally at the top. After passing the test cell, the water is led back into the tank, thereby closing the circuit. The inlet volume flow is monitored by a magnetic-inductive flow sensor. The operating pressure and flow rate can be regulated via the water pump's power supply. The pressure difference Δp is measured using a differential pressure sensor directly connected to the test cell with two tubes (Fig. 12).

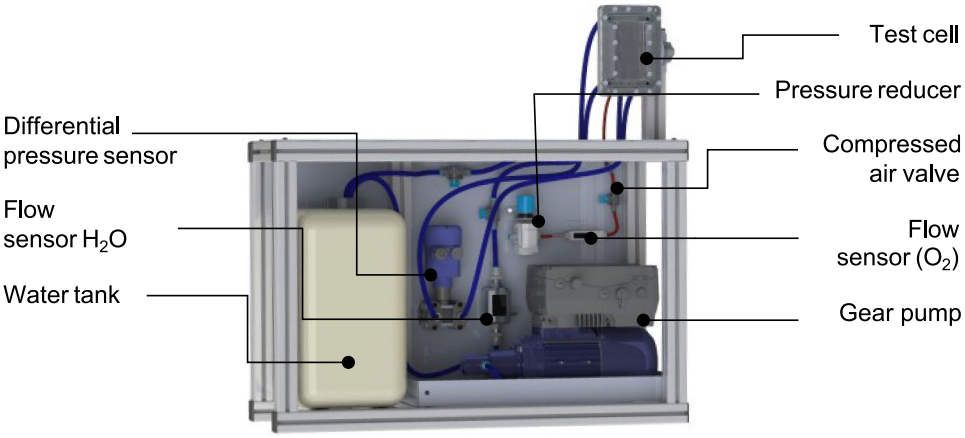

Fig. 12 Top view on flow test bench at IPT with included components

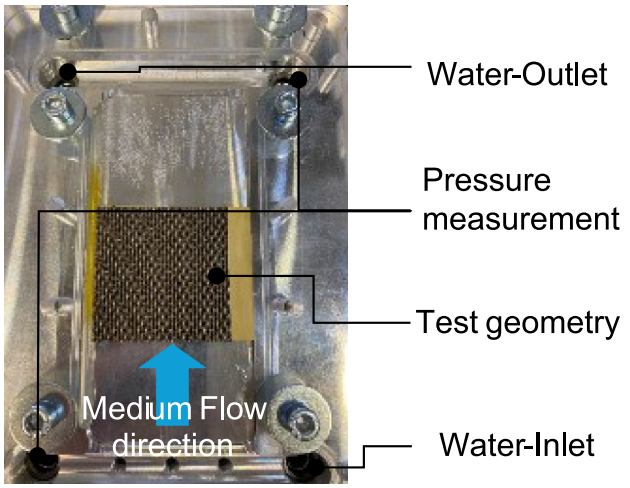

Fig. 13 Top-view on test cell with inserted EMM sample

2.5.1 Procedure

Initially, the pressure drop values are normalized to a sample length of one meter. For testing, one welded sample of 90°_A, 90°_B, 180°_A, and 180°_B each is installed separately into the cell. In Fig. 13, the structure of the test cell with an inserted sample is depicted.

The test cell is oriented horizontally so the influence of the weight on the pressure loss can be neglected. Before testing the different sample series, an unloaded measurement is carried out and pressure losses inherent in the system are deducted in the subsequent measurements. The cell lid is closed and the sample is compressed 0.1 mm in sample height (position controlled). The samples are tested in SWD orientation, i.e., the mesh width (SWD) of the lowest EMM layer (type A) is oriented parallel to the flow direction, and in LWD orientation, i.e., the mesh length (LWD) of the lowest EMM layer (type A) is oriented parallel to the flow direction. The flow rate is varied from 0.2 to 2.2 l/min in steps of 0.2 l/min.

2.6 Simulation model

Since the fluidic phenomena within the PTL structures can be determined experimentally only to a certain extent, a numerical simulation is conducted in addition to the experimental fluidic characterization. Here, ANSYS Fluent is used to analyze the fluidic behavior within the cell.

To describe, analyze, and model the predominant fluid flow in the anode, particularly the pressure field and velocity field, the Navier–Stokes equation for viscous, incompressible fluids is applied [30, 31]:

$$\rho \frac{du_i}{dt} = -\frac{\partial p}{\partial x_i} + \mu \Delta u_i + \rho F_i$$

In this context, ρ represents the fluid density, u is the fluid velocity vector, p is the pressure, μ is the dynamic viscosity, and F represents external forces acting on the fluid, e.g., gravity. The solution of the Navier–Stokes momentum conservation equation is performed considering the continuity equation.

The simulation is carried out for both 90°-orientation and 180°-orientation to draw conclusions on possible effects on media transport and pressure loss.

For input parameters, mesh length, mesh width, sheet thickness, and total thickness of the expanded metal structure are defined according to Table 2. The mesh node width is assumed to be 10% of the mesh length. Based on the generated CAD model, a void volume is generated as part of the simulation preparation, which serves as the process space for the flow simulation. Additionally, a supply and discharge channel of 150 mm is applied to the expanded metals to avoid a possible simulation of backflow and stabilize

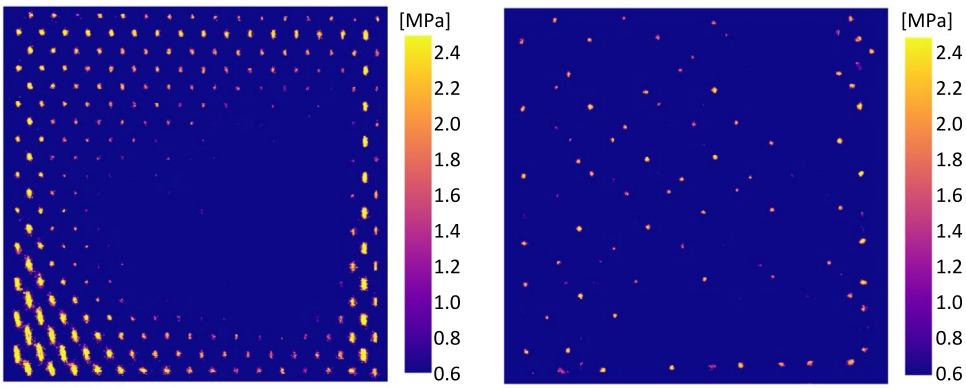

Fig. 14 Heatmaps depicting the contact area (qualitative) and pressure distribution between two EMM type A in 180°-orientation (left) and 90°-orientation (right)

the flow pattern along the mesh size in all geometries. The boundary conditions of the fluid modeling relate to the pressures and fluid velocities determined at the inlet and outlet of the test cell (Figs. 12 and 13). For modeling the inlet, the flow velocity of the process water is 10 cm/s. With an assumed open inflow area of 1.5 mm × 42 mm (63 mm^2), this corresponds to a water volume flow of 380.5 ml/min. Scaled to an assumed square active cell area of 1000 cm^2 and a current density of 2 A/cm^2, the flow rate corresponds to a stoichiometry factor λ of 255 which describes the relation between the actual water flow and the one chemically needed for the electrolysis process. On the output side, only the ambient pressure is specified as a boundary condition for the modeling. A value of 10^{-3} is set as the numerical convergence criterion for all simulations.

3 Results and discussion

The contact area between stacked EMMs is highly dependent on the layer-to-layer orientation. This does not only result in different contact areas, which affect the joining process, the observed mechanical properties and the flow characteristics differ as well. In this paragraph, the respective results gained when joining three-layered EMM PTL through capacitor discharge welding are presented and discussed.

3.1 Deviations in contact area

In Fig. 14, 2D heatmaps of the pressure distribution between two EMMs of type A are presented for 180°-orientation (left) and 90°-orientation (right) of the EMMs.

For 180°-orientation, the contact area is greater than in the case of a 90°-orientation. While for the 180°-orientation where interlocking mesh contact spots with varying shapes are observed (spots in the middle elliptic at edges), the 90°-orientation leads to a print pattern with contact spots

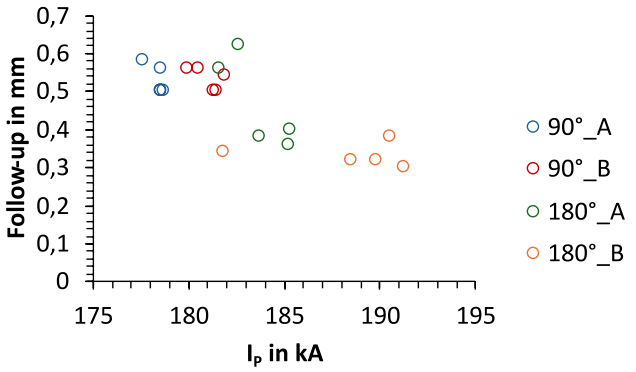

Fig. 15 Left: Follow-up during CD-welding for different sample orientations with regard to peak current strength in kA at constant electrode force

that are different in size. Further, for both orientations, an inhomogeneous pressure distribution is indicated through the different colors with more intense, yellow-colored areas at the edges. (Fig. 14). The imprints indicate a varying contact area between the different layers, and for the CD-welding process, a higher in-plane current density can be expected for a 90°-orientation.

3.2 CD-welding

In Fig. 15 the determined follow-up of the electrodes during welding is plotted against the introduced peak welding current, with regard to parameters *A* and *B*, and EMM orientation. The sample height measured after welding is presented in Fig. 16.

For both variations, the applied welding parameters only show a marginal effect on the follow-up determined during CD welding. But, when applying the same welding parameters, samples with 90°-orientation show a higher follow-up distance than samples with 180°-orientation (Fig. 15). This can be explained when comparing the

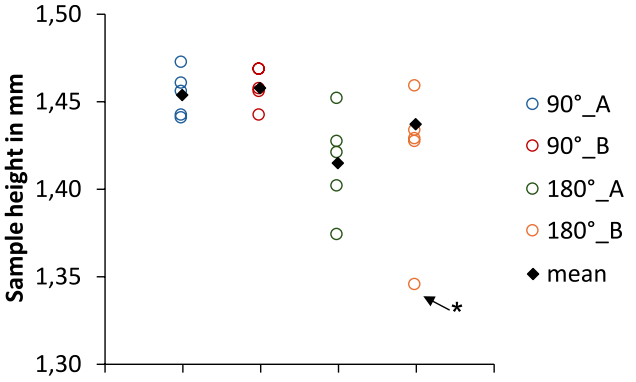

Fig. 16 Sample height in mm determined directly after welding ("*" indicates an outlier, not recognized for calculation of the mean)

different contact area sizes (Fig. 14). For 90°-orientation, the total contact area is smaller compared to 180°-orientation. On one hand, for the resistance welding process, this results in a higher in-plane current density (welding current per area). On the other hand, the difference in contact pressure enhances an imbalance in heat generation, because the contact pressure directly influences the local electric resistance at the points of contact. The higher the local contact pressure, the lower the electric resistance. Thus, resistance heating is more pronounced in areas with poor contact pressure (Fig. 14).

Nevertheless, sample series 90°_A and 90°_B show the greatest sample heights with the lowest deviation after welding (Fig. 16). Here, no significant difference in mean sample height can be observed, and the deviation for both welding parameter sets differs only marginally. Neglecting a single outlier in the sample series 180°_B, the determined sample height of sample series 180°_A has the highest deviation (Fig. 16). The differences in sample height between the different EMM orientations can be explained by the interlocking of the EMM layers in 180°-orientation, which decreases the overall sample height significantly, even before the welding process.

Reflecting light photographs of exemplary welded samples are shown in Fig. 17 (90°-orientation) and Fig. 18 (180°-orientation).

At mesh type A, temper colors can be observed which indicate the occurrence of hot spots during heat input that favor the formation of Ti-oxides appearing in blue. For 90°-orientation, the bluish temper color can be detected at the mesh strand, where the strand is contacting the mid layer (Fig. 17). For 180°-orientation, the bluish color is located closer to the mesh knots, and less dominant, which can again be linked to the lower local welding current density (Fig. 15). The 180°-orientated samples welded with parameter A show the fewest temper colors (Fig. 18).

3.3 Electric resistance

In Fig. 19, the specific electric resistance (μR) determined for 90°-orientation and 180°-orientation is plotted as a function of the applied electrode force (F_{el}) during testing.

With increasing electrode force, µR decreases. At higher electrode forces, the contact area is increased and as a consequence, the electric resistance decreases. At $F_{el} \geq 4$ kN, the electric resistance at 90°-orientation is slightly higher than the electric resistance determined for the 180°-orientation. With regard to the contact area as depicted in Fig. 15, the difference in electric resistance can again be linked to the difference in contact area size. Figuratively, a 180°-orientation of the EMMs appears to be more suitable for increasing the PEM-cell performance through reducing electric resistivity when using an unwelded EMM assembly as PTL. Figure 20 depicts the electric resistance of samples determined after CD welding.

As observed for the unwelded samples, all welded samples show a similar decrease in electric resistance when plotting µR over the applied electrode force. Still, at low electrode forces, the unwelded samples show higher electric resistances ($> 0.015\ \Omega{\cdot}cm^2$) than the welded samples ($< 0.01\ \Omega{\cdot}cm^2$, Figs. 19 and 20). Although a constantly smaller electric resistance is expected for the welded samples, no significant difference in electric resistance can be observed when applying electrode forces of $F_{el} \geq 4$ kN. The latter might be falsified by different amounts of Ti-oxides originating from the welding procedure (Figs. 17 and 18).

While no significant effect in electric resistance can be observed for the different welding parameters and EMM orientation, the sample height is reduced to a different extent during resistance measurements. In Fig. 21, the sample height determined during the electric resistance measurements is plotted as a function of the applied electrode force during the resistance measurements.

While samples with 180°-orientation show a stronger decrease in sample height (−0.03 mm), when increasing the electrode force from 1 to 7 kN, for a 90°-orientation only a marginal decrease in sample height (−0.01 mm) is observed. The determined reduction of the sample height already hints at a difference in mechanical behavior of the 90°- and 180°-orientation of the EMM.

3.4 Compression test

To analyze the mechanical behavior of the PTL with regard to the EMM orientation, quasi-static compression tests are performed. During testing, no failure of the samples is observed. As depicted in Fig. 22, in which the difference in displacement (Δs) is plotted over hysteresis maximum,

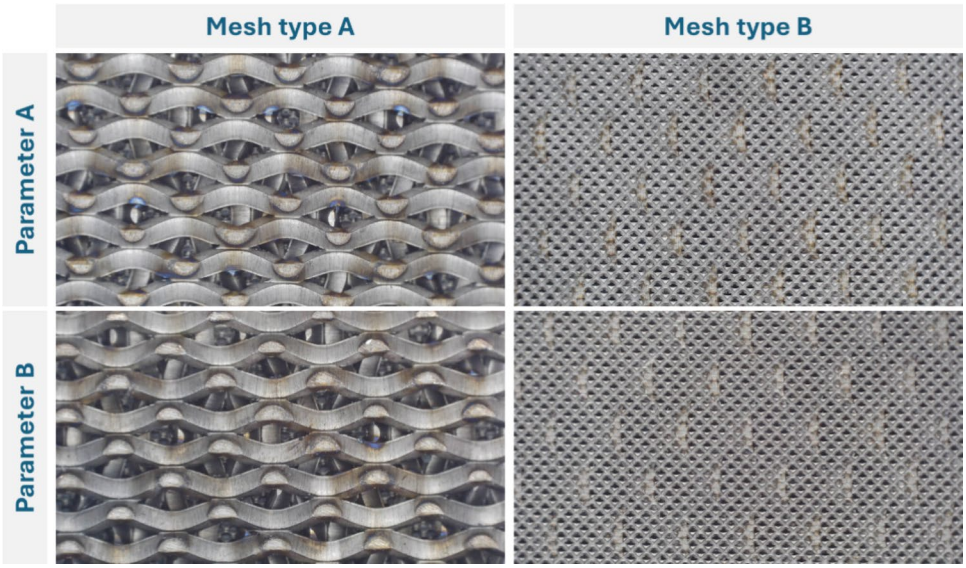

Fig. 17 Reflected light photographs of both sample sites of 90°-orientation with regard to the applied welding parameter set; mesh type A with rough side facing upwards, mesh type B with smooth side facing upwards

Δs differs for the different sample series when separately evaluating the hysteresis loops.

Δs indicates a plastic deformation of the samples, but contrary to the results shown in Fig. 21. The higher Δs, the higher the deformation observed. For 90°-orientation, the decrease in Δs is more pronounced than for 180°-orientation. Although different Δs can be observed for welding parameters A and B for the first hysteresis, the welding parameters seem to have no significant influence on Δs in the case of the second hysteresis. Contrary to that, for 180°-orientation, different Δs can be observed for parameters A and B for both hysteresis (Fig. 22). In general, a higher energy input during welding seems to favor a lower Δs.

After the first hysteresis loop with $F_{max} = 4.5$ kN, Δs is greater than Δs after the second hysteresis loop with $F_{max} = 7$ kN, which indicates a remaining deformation from the first hysteresis and with increasing force a non-linear deformation of the sample can be assumed. Further, for all sample series, the calculated sample standard deviation is significantly greater for the first hysteresis loop (Fig. 22).

Figure 23 presents the calculated work (area within the hysteresis loop) that is converted during the compression test.

For 90°-orientation, and with increasing energy input ($E_{Parameter\ B} > E_{Parameter\ A}$), the work is decreased, indicating a better damping characteristic of the samples with 90°-orientation and for those samples welded with parameter B (Fig. 23). Conversely, this means a higher energy loss for sample series in 180°-orientation. For 90°-orientation, a smaller standard deviation is detectable.

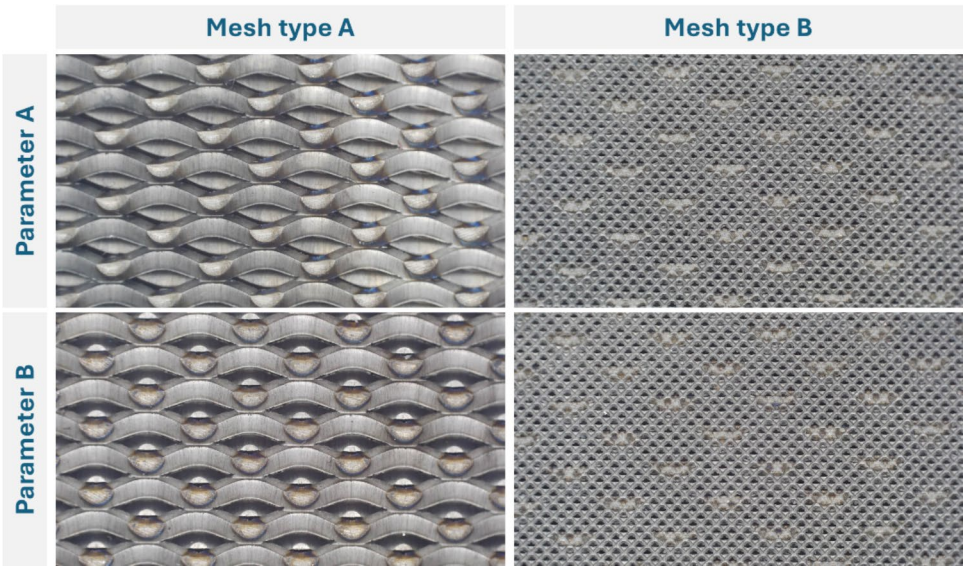

Fig. 18 Reflected light photographs of both sample sites of 180°-orientation with regard to the applied welding parameter set; mesh type A with rough side facing upwards, mesh type B with smooth side facing upwards

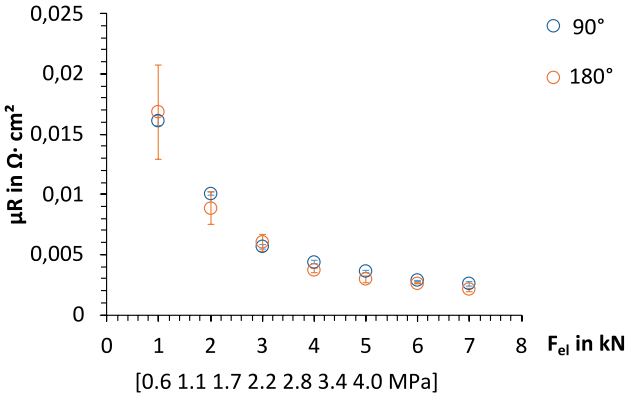

Fig. 19 Specific electric resistance as function of applied electrode force Fel, determined for different unwelded EMM stack-ups regarding a sample area of 17.64 cm^2

3.5 Fluidic characterizations

Figure 24 depicts the determined pressure drop for the different EMM orientations (90°, 180°), welding parameters (*A*, *B*), and sample orientations (SWD, LWD) as a function of the flow rate. Additionally, in Table 4, the sample height after welding is listed for the respective samples that are tested in the flow test.

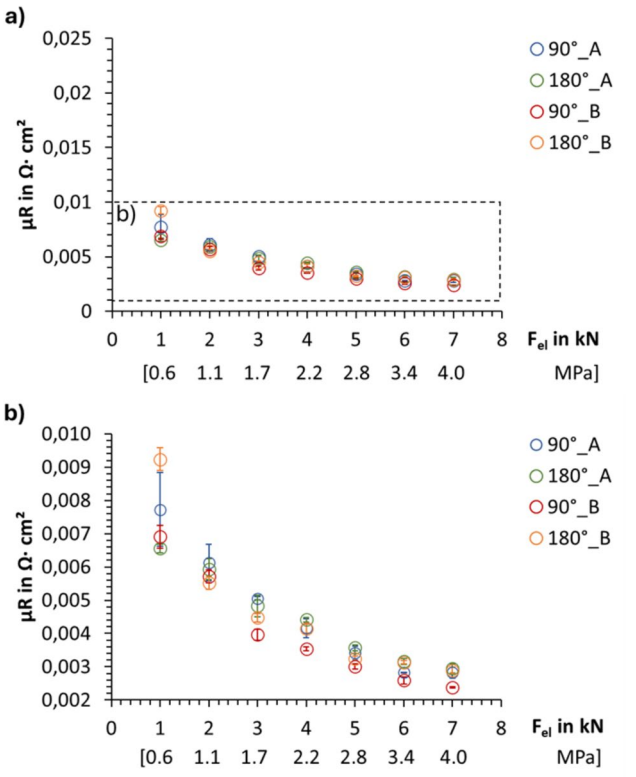

Fig. 20 Specific electric resistance (referred to area 17.64 cm^2) of welded samples with regard to welding parameter (**A**, **B**) and layer orientation (90°, 180°) with enlarged view in (**b**)

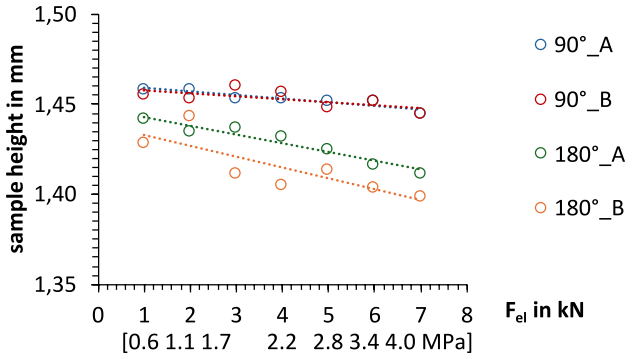

Fig. 21 Sample height over electrode force, measured during determination of electric resistance

For all samples the pressure loss shows an exponential progression. For 180°-orientation, the highest differences with regard to fluidic pressure behavior are observed. While the SWD orientation produces the largest pressure losses within the cell, for LWD orientation the lowest pressure losses are determined (Fig. 24). At a flow rate of 2 l/min, the pressure losses for the LWD orientation are on average 10 times higher than for the SWD orientation. This anisotropy in flow characteristics is also reported by Lafmejani et al. [8] and can be explained by the channel-like structures created by the three-dimensional structure of the expanded metals in the LWD direction, which favor the flow of water.

Samples with 90°-orientation show an orientation dependence of the pressure drop, too. At 2 l/min, the pressure loss of LWD orientation is twice as high as observed for the SWD orientation (Fig. 24). For the samples tested, no clear correlation between welding parameters and pressure loss can be determined. Based on the findings, the orientation direction of the structure within the cell, but also the orientation of the single EMM layers to one another has a significant influence on the pressure drop within an electrolysis cell, even for PTL with reciprocally oriented EMM

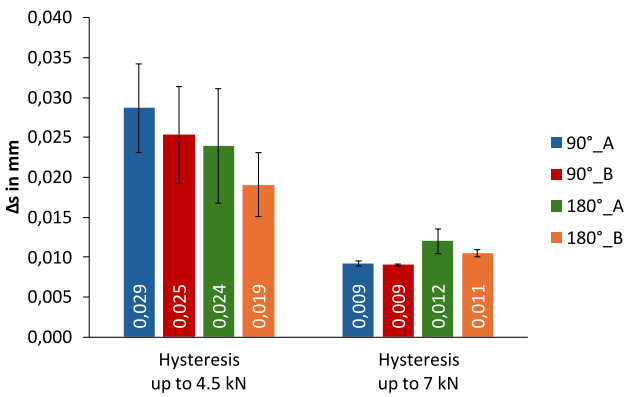

Fig. 22 Determined difference in displacement (Δs) at $F = 25$ N after hysteresis loop up to $F = 4.5$ kN and $F = 7$ kN

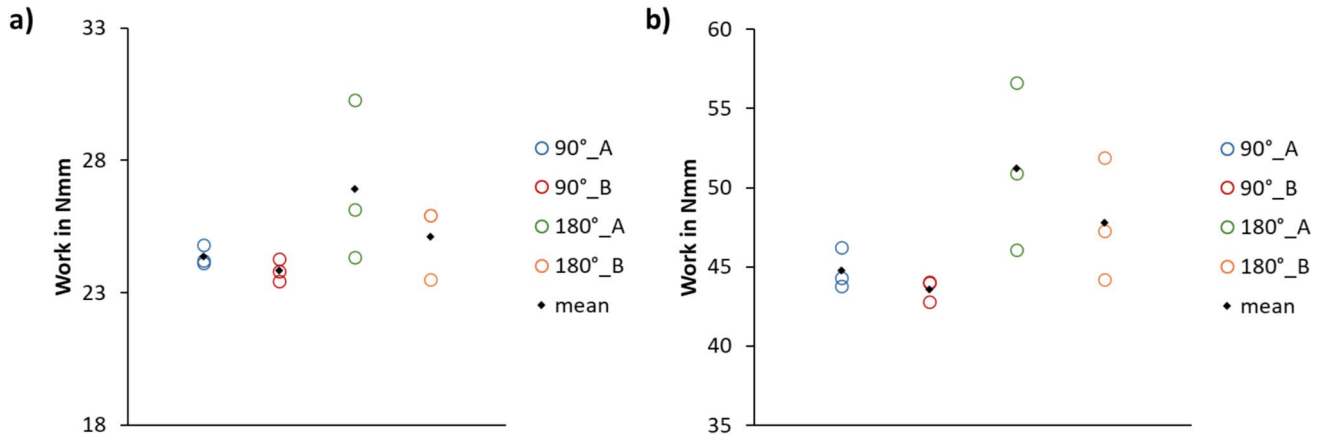

Fig. 23 Calculated area within the hysteresis loop; **a** first hysteresis with *Fmax* = 4.5 kN; **b** second hysteresis with *Fmax* = 7 kN

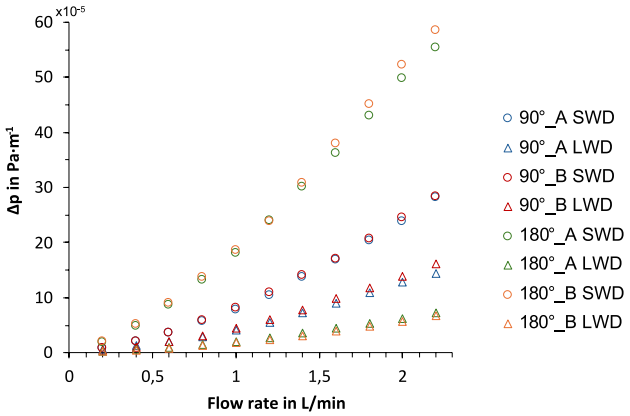

Fig. 24 Pressure loss (Δp) determined for the different samples in SWD and LWD orientation regarding the flow rate

layers. In this case, the pressure drop is reduced when choosing an LWD orientation of the bottom structure (and thus an SWD orientation of the middle structure).

In Fig. 25, the simulation results for 180°-orientation of a two-layered EMM-PTL in LWD flow orientation are presented. Respective results for a 90°-orientation are shown in Fig. 26.

The simulation results show slightly different flow velocities for 90°- and 180°-orientation, but significant differences in the flow paths are revealed. For 180°-orientation, where the flow direction is parallel to LWD of all EMM layers, isolated turbulences occur within the mesh opening, directly after passing a mesh knot in LWD direction (Fig. 25). The maximum calculated velocity is 0.44 m/s, while green visualized velocity streamlines are dominant (0.22 m/s). Contrary, more pronounced turbulences (dark blue) and a greater deflection of the flow paths are visible for the 90°-orientation (Fig. 26). Consequently, an increased velocity distribution is determined with a maximum velocity of 0.49 m/s and results in a higher pressure drop as observed in flow tests (Fig. 24).

Transferring the results concerning the flow characteristics throughout the structures, the intended use of multi-layered EMM composites as PTL in PEM electrolysis, the orientation of the EMMs are of high importance, although it becomes apparent both tested orientations bear their own possible advantages regarding cell PTL functionality. A 90°-orientation might enhance medium transport towards the membrane, when oriented properly, i.e., the smooth side of every EMM layer that is contained is faced towards the membrane. As reported in previous research, the removal of gas bubbles is of high importance and their accumulation is primary reported to be within the areas of turbulence [8]. Here, the results for the 180°-orientation promises a clear advantage over a 90°-orientation of the EMM layers because and improved bubble removal is assumed because of the lower extent of turbulences (Figs. 25 and 26).

Table 4 Height of samples analyzed in flow test, determined directly after welding

Sample	Height in mm
90°_A	1.44
90°_B	1.47
180°_A	1.40
180°_B	1.46

4 Conclusions

In this work, the effects of EMM layer orientation in EMM PTL for PEM electrolysis on the CD welding process and resulting differences in PTL characteristics were investigated. Based on the results, the following conclusions are drawn.

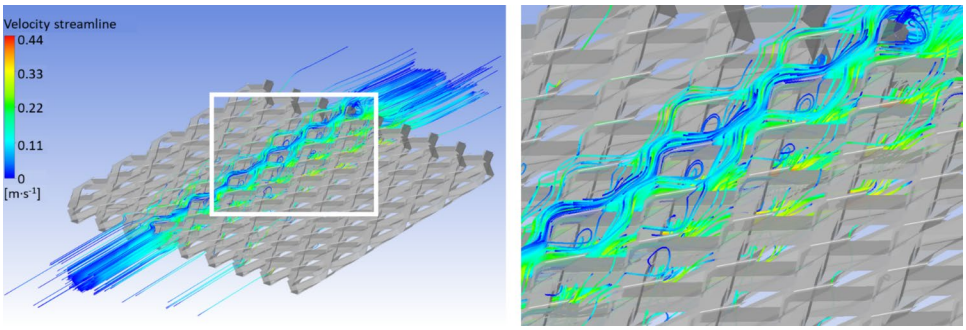

Fig. 25 Simulation of velocity streamlines across two-layered EMM PTL with 180°-orientation and flow direction parallel to LWD

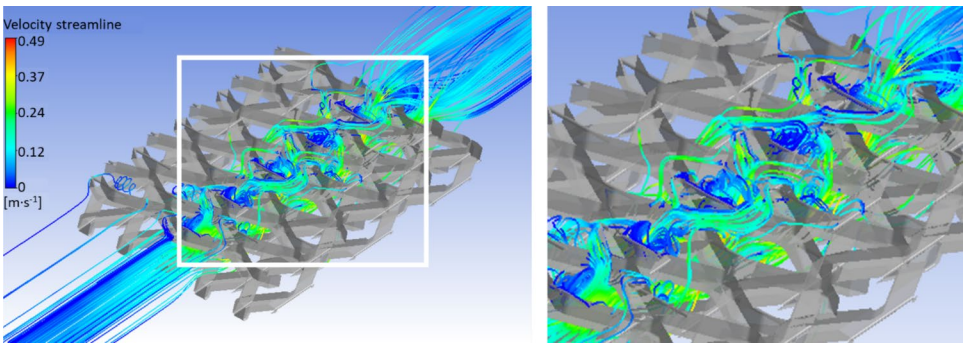

Fig. 26 Simulation of velocity streamlines across two-layered EMM PTL with 90°-orientation and flow direction parallel to LWD

- In CD-welding, the layer-to-layer orientation of the EMM defines the respective contact areas and therefore influences the local current density. Local deviations in pressure distribution result in differences in resistive heating and hence, in local current densities. The resulting inhomogeneous heat distribution can alter the reproducibility of the sample height and should be avoided through a consistent stacking of the layers.
- CD welding is suitable to join multiple EMMs in a single step with minimal Ti-oxide formation. But, resistance heating should be as homogeneous as possible to avoid local heat peaks which can favor local oxide formation during welding and hence, can decrease the PTL resistance against degradation processes, especially corrosion.
- The electric resistance of welded samples decreases when increasing the electrode force, and figuratively with increasing clamping pressure. At high electrode forces, the difference in electric resistance is negligible and no significant correlation between the EMM orientation and electric resistance can be detected. But, at lower electrode forces, the welded samples show a significantly lower electric resistance bearing the possibility for decreasing the cell clamping pressure for less mechanical stress at the membrane while maintaining cell efficiency.
- The compression tests reveal a higher energy absorption in the case of a 180°-orientation of the EMMs, while the damping characteristics of the samples with a 90°-orientation are improved comparatively.
- In flow tests with single-phase medium flow, samples with 180°-orientation show the lowest pressure loss when the flow direction is parallel to LWD, but the highest pressure difference when the flow direction is perpendicular to LWD. Here, Δp is increased by a factor of ten. In general, the flow direction parallel to LWD of the bottom layer leads to smaller pressure drops.
- Based on the simulation results of the fluid dynamics across the EMM stack, turbulences are more likely to occur at 90°-orientation. The deflection of the flow path around mesh strands at 90°-orientation, which is significantly less pronounced in 180°-orientation, increases Δp but possibly improves medium transport towards the membrane when being assembled as PTL in an electrolysis cell. Contrary, for 180°-orientation, an even smaller Δp hints at better gas removal and might hinder the accumulation of gas bubbles within the mesh structures because of fewer turbulences.

Author contribution The authors, Maike Epperlein, Martin Aretz, Alexander Schiebahn, and Uwe Reisgen, declare that the uploaded document is not covered by a copyright other than the authors.

Funding Open Access funding enabled and organized by Projekt DEAL. The research project "HyInnoLyze2 - Dynamik und Degradation von skalierten Systemen" (03ZU2115AC) is funded by the Federal Ministry of Research, Technology and Space as part of the innovation

network “Clusters 4 Future” on the basis of a resolution of the German Bundestag. The project is led by PT Jülich, Forschungszentrum Jülich GmbH, Wilhelm-Johnen-Straße, 52428 Jülich and carried out at the Forschungszentrum Jülich, Jülich, Germany, the RWTH Aachen University, Welding and Joining Institute, Aachen, Germany and the Fraunhofer Institute for Production Technology, Aachen, Germany, together with partners from industry.

Data availability Data generated during the current study is available from the corresponding author on reasonable request.

Declarations

Competing interests The authors declare no competing interests.

References

1. Locci C, Mertens M, Höyng S, Schmid G, Bagus T, Lettenmeier P (2024) Scaling-up PEM electrolysis production: challenges and perspectives. Chem Ing Tech 96:22–29. https://doi.org/10.1002/cite.202300111
2. Andrea Lübcke. Wasserstoff-Kompass. www.wasserstoff-kompass.de/. Accessed 27 Jun 2024
3. Thomassen MS, Reksten AH, Barnett AO, Khoza T, Ayers K (2021) PEM water electrolysis. In: T. Smolinka, J. Garche, editors. Electrochemical power sources: fundamentals, systems, and applications: Elsevier. p. 199–228. https://doi.org/10.1016/B978-0-12-819424-9.00013-6
4. Dilthey U (2006) Schweiß- und Schneidtechnologien, 3rd ed. Springer, Berlin
5. Epperlein M, Schiebahn A, Reisgen U (2024) Fügen von Gasdiffusionsschichten durch Widerstandsschweißen für eine Ressourcen schonende Produktion von Wasserstoffelektrolyseuren. DVS-Berichte 395:329–340
6. Scott K, Argyropoulos P, Yiannopoulos P, Taama WM (2001) Electrochemical and gas evolution characteristics of direct methanol fuel cells with stainless steel mesh flow beds. J Appl Electrochem. https://doi.org/10.1023/A:1017559124395
7. Iwaniszyn M, Sindera K, Gancarczyk A, Leszczyński B, Korpyś M, Suwak M et al (2022) Characterization of fluid flow and heat transfer of expanded metal meshes for catalytic processes. Energies 15:8437. https://doi.org/10.3390/en15228437
8. Lafmejani SS, Müller M, Olesen AC, Kær SK (2018) Experimental and numerical study of flow in expanded metal plate for water electrolysis applications. J Power Sources 397:334–342. https://doi.org/10.1016/j.jpowsour.2018.07.032
9. Fallah Vostakola M, Ozcan H, El-Emam RS, Amini Horri B (2023) Recent advances in high-temperature steam electrolysis with solid oxide electrolysers for green hydrogen production. Energies 16:3327. https://doi.org/10.3390/en16083327
10. Frey H (2023) Energieträger Wasserstoff. Springer Vieweg Springer Fachmedien Wiesbaden GmbH, Wiesbaden
11. Smolinka T, Garche J (2022) Electrochemical power sources: fundamentals, systems, and applications - hydrogen production by water electrolysis. Elsevier B.V.
12. Smith D, Graciano C, Martínez G (2021) Expanded metal: a review of manufacturing, applications and structural performance. Thin-Walled Struct 160:107371. https://doi.org/10.1016/j.tws.2020.107371
13. Deutsches Institut für Normung e.V. (1967) DIN 791:1967–03: Streckgitter. DIN Media GmbH
14. Wang A, Yuan W, Huang S, Tang Y, Chen Y (2017) Structural effects of expanded metal mesh used as a flow field for a passive direct methanol fuel cell. Appl Energy 208:184–194. https://doi.org/10.1016/j.apenergy.2017.10.052
15. McLeod AJ, Bühre LV, Bensmann B, Herrera OE, Mérida W (2024) Anode and cathode overpotentials under accelerated stress testing of a PEM electrolysis cell. J Power Sources 589:233750. https://doi.org/10.1016/j.jpowsour.2023.233750
16. Kurzweil P (2023) Chemie: Grundlagen, technische Anwendungen, Rohstoffe, Analytik und Experimente, 12th ed. Springer Vieweg, Wiesbaden, Heidelberg
17. Linnemann M, Peltzer J (2022) Wasserstoffwirtschaft kompakt. Springer Fachmedien Wiesbaden, Wiesbaden
18. Selamet OF, Ergoktas MS (2015) Effects of bolt torque and contact resistance on the performance of the polymer electrolyte membrane electrolyzers. J Power Sources 281:103–13. https://doi.org/10.1016/j.jpowsour.2015.01.162
19. Marangio F, Santarelli M, Cali M (2009) Theoretical model and experimental analysis of a high pressure PEM water electrolyser for hydrogen production. Int J Hydrogen Energy 34:1143–1158. https://doi.org/10.1016/j.ijhydene.2008.11.083
20. Ma S, Li L, Kohama R, Nakajima H, Ito K (2024) Effects of temperature and pressure on the limiting current density of PEM electrolysis cells based on a theoretical prediction model and experiments. Int J Hydrogen Energy 71:1428–1441. https://doi.org/10.1016/j.ijhydene.2024.05.345
21. Höh M A (2017) Porous transport layers for polymer electrolyte membrane water electrolyzers. Dissertation RWTH Aachen University. https://doi.org/10.18154/RWTH-2017-09280
22. Borgardt E, Giesenberg L, Reska M, Müller M, Wippermann K, Langemann M et al (2019) Impact of clamping pressure and stress relaxation on the performance of different polymer electrolyte membrane water electrolysis cell designs. Int J Hydrogen Energy 44:23556–67. https://doi.org/10.1016/j.ijhydene.2019.07.075
23. Holtwerth S (2022) Mechanisches Verhalten von Polymer-Elektrolyt-Membran-Elektrolysezellen und -Stacks. Dissertation, RWTH Aachen University. https://doi.org/10.18154/RWTH-2023-04311
24. SHAANXI LASTING TITANIUM INDUSTRY CO., LTD (2023) Quality Certificate Acc. EN10204/3.1+PED 2014/68/EU: Titanium Coil Gr.1
25. Müller U (2015) Gas diffusion electrode. Patent 20160049677. MeliCon GmbH
26. Fujifilm Germany. Druckmessfolie. 15.04.2025. www.fujifilm.com/de/de/business/inspection/measurement-film/prescale/feature. Accessed 17 Apr 2025
27. DVS – Deutscher Verband für Schweißen und verwandte Verfahren e. V. (2016) DVS 2911: Kondensatorentladungsschweißen - Grundlagen, Verfahren und Technik. DVS Media GmbH
28. DVS – Deutscher Verband für Schweißen und verwandte Verfahren e. V. (2014) DVS 2929–1: Messung des Übergangswiderstandes: Grundlagen, Messmethoden und Einrichtungen. DVS Media GmbH

29. Deutsches Institut für Normung e.V. (2023) DIN 50106:2023-02: Prüfung metallischer Werkstoffe – Druckversuch bei Raumtemperatur. Beuth Verlag Berlin
30. Rein M (2020) Einführung in die Strömungsmechanik: Elementare Grudlagen und Beispiele. Universitätsverlag Göttingen
31. White FM (2011) Fluid mechanics, 7th ed. McGraw-Hill, New York